Tracking Refractivity from Clutter Using Kalman and Particle Filters

Caglar Yardim, *Member, IEEE*, Peter Gerstoft, and William S. Hodgkiss, *Member, IEEE*

***Abstract*—We address the problem of tracking the spatial and temporal lower atmospheric variations in maritime environments. The evolution of the range and height-dependent index of refraction is tracked using the sea clutter return from sea-borne radars operating in the region. A split-step fast Fourier transform based parabolic equation approximation to the wave equation is used to compute the clutter return in complex environments with varying index of refraction. In addition, regional statistics are incorporated as prior densities, resulting in a highly nonlinear and non-Gaussian tracking problem. Tracking algorithms such as the extended Kalman, unscented Kalman and particle filters are used for tracking both evaporative and surface-based electromagnetic ducts frequently encountered in marine environments. The tracking performances and applicability of these techniques to different types of refractivity-from-clutter problems are studied using the posterior Cramér-Rao lower bound. Track divergence statistics are analyzed. The results show that while the tracking performance of the Kalman filters is comparable to the particle filters in evaporative duct tracking, it is limited by the high non-linearity of the parabolic equation for the surface-based duct case. Particle filters, on the other hand, prove to be very promising in tracking a wide range of environments including the abruptly changing ones.**

***Index Terms*—Atmospheric ducts, extended Kalman filter (EKF), parabolic equation, particle filter (PF), refractivity-from-clutter (RFC), spatial and temporal tracking, unscented Kalman filter (UKF).**

I. Introduction

NON-STANDARD electromagnetic propagation due to formation of lower atmospheric sea ducts is a common occurrence in maritime radar applications. Under these conditions, some fundamental system parameters of a sea-borne radar can deviate significantly from their original values specified assuming standard-air (0.118 M-units/m) conditions. These include the variation in the maximum operational range, creation of regions where the radar is practically blind (radar holes), and increased sea surface clutter. Therefore, it is important to predict the real-time 3-D environment the radar is operating in so that the radar operator will at least know the true system limitations and in some cases even compensate for them.

The environment is characterized by the modified refractivity profile (M-profile) and there are many techniques that measure or predict the lower atmospheric index of refraction. Some of the conventional techniques include radiosondes and rocketsondes that estimate the index of refraction by measuring the vertical temperature, humidity and pressure profiles, microwave refractometers that measure the index of refraction using cavity resonators, and meteorological models such as the Coupled Ocean/Atmospheric Mesoscale Prediction System (COAMPS) that give M-profile forecasts [1]–[3]. There also are other techniques that can refer the refractivity using lidar [4] and GPS [5] measurements.

However, it also is possible to predict the duct properties using the radar itself. When launched at a low elevation angle, the electromagnetic signal will be trapped within the duct which can be taken as a range-dependent leaky waveguide bounded from below by the sea surface. This will result in multiple reflections and strong interaction with the surface which in turn will result in an increase in the sea clutter, forming clutter rings. This normally unwanted portion of the received signal then can be used to infer the environment that gives such a clutter structure. These techniques can be classified as refractivity-from-clutter (RFC) techniques [6]–[13]. More detailed discussions about the differences between the RFC schemes can be found in [12], [13].

This paper is a natural extension to these previous RFC methods which compute the 2-D range and height-dependent M-profile for a given azimuth direction. Instead of inverting the environmental parameters for a given azimuth and time, the emphasis here is on tracking both the temporal and spatial evolutions of duct parameters. Throughout this paper, the term spatial evolution is used to represent the evolution of the 2-D M-profile with the rotating azimuth of the radar. This is achieved by employing tracking filters. The problem is formulated in a Kalman framework, where the clutter for a given environment is calculated using a split-step fast Fourier transform (FFT) based parabolic equation (PE) approximation to the wave equation [14]. This introduces a high level of nonlinearity in the measurement equation. The problem then is solved by using the following three algorithms.

1) Extended Kalman filter (EKF), where the measurement equation is linearized using the first order Taylor series expansion.
2) Unscented Kalman filter (UKF), where the nonlinearity in the parabolic equation is kept but the probability density functions (pdf) are restricted to be Gaussian.

Manuscript received May 29, 2007; revised August 28, 2007. This work was supported by the Office of Naval Research Code 32, under Grant N00014-05-1-0369.

C. Yardim was with the Electrical and Computer Engineering Department, University of California, San Diego, La Jolla, CA 92093 USA and also with the Marine Physical Laboratory, Scripps Institution of Oceanography, University of California, San Diego, La Jolla, CA 92093-0238 USA. He is now with the Marine Physical Laboratory, Scripps Institution of Oceanography, University of California, San Diego, La Jolla, CA 92093-0238 USA (e-mail: cyardim@ucsd.edu).

P. Gerstoft and W. S. Hodgkiss are with the Marine Physical Laboratory, Scripps Institution of Oceanography, University of California, San Diego, La Jolla, CA 92093-0238 USA (e-mail: gerstoft@ucsd.edu; whodgkiss@ucsd.edu).

Color versions of one or more of the figures in this paper are available online at http://ieeexplore.ieee.org.

Digital Object Identifier 10.1109/TAP.2008.919205

3) Particle filter (PF) or sequential Monte Carlo (SMC), which uses a sequential importance resampling (SIR) or bootstrap filter to track the nonlinear, non-Gaussian system.

II. Theory

Two equations are necessary to fully characterize the dynamic system; one that describes the evolution of the lower atmosphere and another that governs the propagation of the electromagnetic signal in this environment. At a time step k, these equations can be given as follows:

$$\mathbf{x}_k = \mathbf{F}\mathbf{x}_{k-1} + \mathbf{v}_{k-1} \tag{1}$$

$$\mathbf{y}_k = \mathbf{h}(\mathbf{x}_k) + \mathbf{w}_k \tag{2}$$

where $\mathbf{F}$ is a known linear function of the state vector $\mathbf{x}_k$, $\mathbf{h}(\cdot)$ is a known nonlinear function of the measurement vector $\mathbf{y}_k$, $\mathbf{v}_k$ and $\mathbf{w}_k$ are the process and the measurement noise vectors, respectively with

$$\begin{aligned} &\mathrm{E}\left\{\mathbf{v}_k\mathbf{v}_i^T\right\} = \mathbf{Q}_k\delta_{ki} \quad \mathrm{E}\left\{\mathbf{v}_k\mathbf{w}_i^T\right\} = \mathbf{0} \quad \forall i,k \\ &\mathrm{E}\left\{\mathbf{w}_k\mathbf{w}_i^T\right\} = \mathbf{R}_k\delta_{ki}. \end{aligned} \tag{3}$$

The state vector $\mathbf{x}_k$ is composed of the n_{x} parameters that describe the complex environment at the step index k. The state vector is constructed (Appendix A) depending on the type of the duct (evaporation/surface-based duct (SBD)/mixed) and the appropriate model (range-dependent/independent). The process noise $\mathbf{v}_k$ is taken as a zero-mean Gaussian pdf. The prior density $\mathrm{p}(\mathbf{x}_o)$ usually is constructed using the regional statistics. This density must be Gaussian for the Kalman filters. It can be any distribution for the PF. For temporal tracking, k usually is in terms of minutes and for spatial tracking it is in terms of azimuth of the rotating radar.

Equation (1) is the state equation for the stochastic environmental model. $\mathbf{F}$ is the linear state transition matrix which will be taken as the identity matrix following Appendix B. The main assumption is that the environment is changing slowly compared to the step index. Although the M-profile is not expected to vary considerably in short intervals, sudden fluctuations can occur and the filters will require larger $\mathbf{Q}_k$ to perform adequately in these environments.

Equation (2) is the measurement equation and it relates the environment given by $\mathbf{x}_k$ to the radar clutter power $\mathbf{y}_k$ through a highly nonlinear $\mathbf{h}(\cdot)$ function which uses a split-step FFT-PE, see Appendix C. Usually, the nonlinearity is less severe for evaporative ducts, however the degree of nonlinearity and hence the filter performance still heavily depends on the current location of $\mathbf{x}_k$ on the state-space. $\mathbf{w}_k$ is the logarithm of the sea surface radar cross-section (RCS), see Appendix C.

There are many successful models for the sea clutter distribution. The selection of the appropriate model depends mainly on the grazing angle, radar resolution and sea roughness. Some of the commonly used models include the Rayleigh, Weibull, log-normal and K-distributed sea clutter [15], [16]. Since the Kalman framework requires Gaussian distributions, the model can only be constructed if the sea clutter is selected as log-normal even if this may not be the most suitable pdf. The PF does not have such restrictions and any pdf can be used. However, since it is desirable to compare these filters under the same set of assumptions, sea clutter is taken as log-normal.

Note that no other noise terms are used, so all the variation in the signal is represented by the additive $\mathbf{w}_k$ in the logarithmic domain. This assumption is made due to the dominant effect of the increased sea clutter resulting from the entrapment of the electromagnetic signal inside the duct. However, this assumption may have to be modified for a low SNR system. Alternatively, one can use a measurement equation based on the formulation given in [12].

A. Tracking Algorithms

1) Extended Kalman Filter: Since the tracking problem given in (1), (2) is nonlinear with non-Gaussian pdf, a Kalman filter (KF) cannot be used. Instead, an extended Kalman filter (EKF) [17] is used by locally linearizing the equations using the first terms in the Taylor series expansions of the nonlinear transformations (such as $\mathbf{h}$) and assuming that the nonlinearities are small so that EKF will perform well. Since the pdfs are Gaussian and the equations are linearized, it is necessary to propagate only the mean and covariance as in the KF. However, due to this approximation, the EKF cannot claim the optimality enjoyed by the KF for linear-Gaussian systems. The EKF has been implemented successfully in a large number of applications such as radar and sonar target tracking applications and its speed and ease of implementation makes the EKF the filter of choice. Therefore, the EKF is the first filter tested in the RFC tracking problem.

2) Unscented Kalman Filter: To alleviate some of the linearization problems confronting the EKF, the unscented Kalman filter (UKF) [18], [19] has been introduced. Unlike the EKF which enforces linearity, this filter enforces Gaussianity and keeps the nonlinearity. This still enables the filter to carry all the necessary information by propagating only the mean and covariance as does the KF. It uses an unscented transformation (UT) that enables the propagation of the mean and variance through nonlinear functions. The UKF represents initial densities using only a few predetermined particles called sigma points. These points are chosen deterministically by the UT algorithm and they describe accurately the mean and covariance of a pdf. As the random variable undergoes a nonlinear transformation, these points are propagated through this nonlinear function and used to reconstruct the new mean and covariance using the UT weights. Hence, unlike the EKF, they can compute accurately the mean and covariance to at least second order (third if the initial pdf is Gaussian) of the nonlinearity. Although it is fast relative to more advanced techniques, derivative-free, and an improvement over the EKF, there still are two weaknesses. The first is that the nonlinearity may be so severe that it may require an even higher order accuracy than the UKF can provide to correctly capture the mean and covariance. The other is that the densities may be highly non-Gaussian so that the first two moments will not be sufficient even if they can be calculated correctly. The UKF used throughout this work is summarized in Appendix D.

3) Particle Filter: The last algorithm used in this paper is the sequential Monte Carlo (SMC) or the particle filter (PF). This filter does not come with any inherent assumptions and is used for many nonlinear, non-Gaussian tracking problems [20]. The main difference with Kalman type filters is that, since no Gaussian assumption is made, propagating the mean and covariance is not sufficient. Instead the PF propagates an ensemble of particles to represent the densities. These particles are selected randomly by MC runs. Compared with the sigma points of the UKF, a much larger number of particles are needed to represent the pdf. Therefore, the PF can perform much better than its KF variants but it does this with an order of magnitude increase in the required computational resources. There are many different variants of the PF such as the regularized particle filter (RPF), Markov chain Monte Carlo step particle filter (MCMC-PF), auxiliary (ASIR) and classical sequential importance resampling (SIR) particle filter [21].

The SIR algorithm is used throughout this work. Normally, degeneracy can be a problem for the SIR algorithm, especially for low process noise systems. However, due to the environmental uncertainty in the model (Appendix B), $\mathbf{Q}_k$ is selected relatively large, thus mostly eliminating the need for more complex particle filters with improved sample diversity. The SIR algorithm [22] is summarized in Appendix D.

B. Posterior Cramér-Rao Lower Bound

It usually is not possible to have an optimal estimator with minimum mean square error (MMSE) for the nonlinear filtering problems such as RFC. All the techniques used in this paper also are sub-optimal techniques. Therefore, it is desirable to have a tool that not only can assess the performances of these sub-optimal techniques but also provide a limit to achievable performance for a given environment.

In a classical non-Bayesian framework, the Cramér-Rao lower bound (CRLB), which is the inverse of the Fisher information matrix (FIM), is commonly used. In a Bayesian framework this instead can be replaced by the posterior CRLB (PCRLB) introduced by van Trees [23]. Since this paper exclusively works with PCRLB, it will henceforth be referred to simply as CRLB.

Any filter that achieves a mean square error (MSE) equal to the CRLB is called an efficient estimator. For a linear and Gaussian system, the Kalman filter is an efficient estimator. It may not be possible to attain the CRLB for a nonlinear, non-Gaussian system.

Let $\mathbf{J}_k$ be the inverse of the CRLB_k as a $(n_\mathrm{x} \times n_\mathrm{x})$ filtering information matrix so that the MSE of any filter estimate at tracking step index k will be bounded as

$$\mathrm{E}\left\{(\widehat{\mathbf{x}}_{k|k} - \mathbf{x}_k)(\widehat{\mathbf{x}}_{k|k} - \mathbf{x}_k)^T\right\} \geq \mathbf{J}_k^{-1} \tag{4}$$

where $\widehat{\mathbf{x}}_{k|k}$ is the estimate of $\mathbf{x}_k$ given its previous history $\{\mathbf{x}_o, \mathbf{x}_1, \ldots, \mathbf{x}_{k-1}\}$ and the set of measurements $\{\mathbf{y}_1, \mathbf{y}_2, \ldots, \mathbf{y}_k\}$. A computationally efficient way of computing this CRLB recursively for discrete-time nonlinear filtering problems is [24]

$$\mathbf{J}_k = \mathbf{D}_{k-1}^{22} - \left[\mathbf{D}_{k-1}^{12}\right]^T \left(\mathbf{J}_{k-1} + \mathbf{D}_{k-1}^{11}\right)^{-1} \mathbf{D}_{k-1}^{12} \tag{5}$$

where

$$\mathbf{D}_{k-1}^{11} = -\mathrm{E}\left\{\nabla_{\mathbf{x}_{k-1}} \left[\nabla_{\mathbf{x}_{k-1}} \log \mathrm{p}(\mathbf{x}_k|\mathbf{x}_{k-1})\right]^T\right\} \tag{6}$$

$$\mathbf{D}_{k-1}^{12} = -\mathrm{E}\left\{\nabla_{\mathbf{x}_k} \left[\nabla_{\mathbf{x}_{k-1}} \log \mathrm{p}(\mathbf{x}_k|\mathbf{x}_{k-1})\right]^T\right\} \tag{7}$$

$$\mathbf{D}_{k-1}^{22} = -\mathrm{E}\left\{\nabla_{\mathbf{x}_k} \left[\nabla_{\mathbf{x}_k} \log \mathrm{p}(\mathbf{x}_k|\mathbf{x}_{k-1})\right]^T\right\} - \mathrm{E}\left\{\nabla_{\mathbf{x}_k} \left[\nabla_{\mathbf{x}_k} \log \mathrm{p}(\mathbf{y}_k|\mathbf{x}_k)\right]^T\right\}. \tag{8}$$

Note that the computations only require $(n_\mathrm{x} \times n_\mathrm{x})$ matrices and the computation cost is independent of the step index k.

The RFC tracking problem with the system of equations defined in (1), (2) has a linear state equation and both of the random noise sequences $\mathbf{v}$ and $\mathbf{w}$ are additive and Gaussian. Therefore, the above equations can be reduced to

$$\begin{aligned} &\mathbf{D}_{k-1}^{11} = \mathbf{F}^T \mathbf{Q}_{k-1}^{-1} \mathbf{F} \quad \mathbf{D}_{k-1}^{12} = -\mathbf{F}^T \mathbf{Q}_{k-1}^{-1} \\ &\mathbf{D}_{k-1}^{22} = \mathbf{Q}_{k-1}^{-1} + \mathrm{E}\left\{\mathbf{H}_k^T \mathbf{R}_k^{-1} \mathbf{H}_k\right\} \end{aligned} \tag{9}$$

where

$$\mathbf{H}_k = \left[\nabla_{\mathbf{x}_k} \mathbf{h}^T(\mathbf{x}_k)\right]^T \tag{10}$$

is the Jacobian of $\mathbf{h}(\mathbf{x})$ evaluated at its true value $\mathbf{x}_k$. Unfortunately the expectation in (9) has to be evaluated numerically. The recursion in (5) is initiated by using the prior probability $\mathrm{p}(\mathbf{x}_\mathrm{o})$ to compute $\mathbf{J}_o$ as

$$\mathbf{J}_\mathrm{o} = -\mathrm{E}\left\{\nabla_{\mathbf{x}_\mathrm{o}} \left[\nabla_{\mathbf{x}_\mathrm{o}} \log \mathrm{p}(\mathbf{x}_\mathrm{o})\right]^T\right\} = \mathbf{P}_\mathrm{o}^{-1} \tag{11}$$

where $\mathbf{P}_\mathrm{o}$ is the covariance of the prior density, assuming it is Gaussian.

III. Examples

This section is composed of three synthetic and one experimental examples covering the spatial and temporal tracking of both evaporative and surface-based ducts. Throughout the examples, issues such as the performance limitations, filter efficiencies, divergence characteristics, and CPU time comparisons are addressed. These four case studies are as follows.

1) Temporal tracking of a fixed path, range-independent surface-based duct (SBD) for performance comparison of the EKF, UKF, and PF with respect to the CRLB.
2) Divergence analysis of the EKF, UKF and PF for a typical temporal range-independent SBD tracking problem.
3) Temporal tracking of a range-dependent littoral evaporation duct. Comparison with the SBD tracking.
4) Spatial tracking of the SBD from the Wallops'98 experiment, using the SPANDAR clutter data.

A. Case Study I: Temporal Tracking of a Range-Independent Surface-Based Duct

This example is used to compare the tracking performances of the EKF, UKF, and PF and compute their efficiencies using the numerically computed CRLB. The range-independent SBD is selected from the environmental library of the Advanced Refractive Effect Prediction System (AREPS) [25]. The Bahrain radiosonde station in the Persian Gulf is used for the simulation

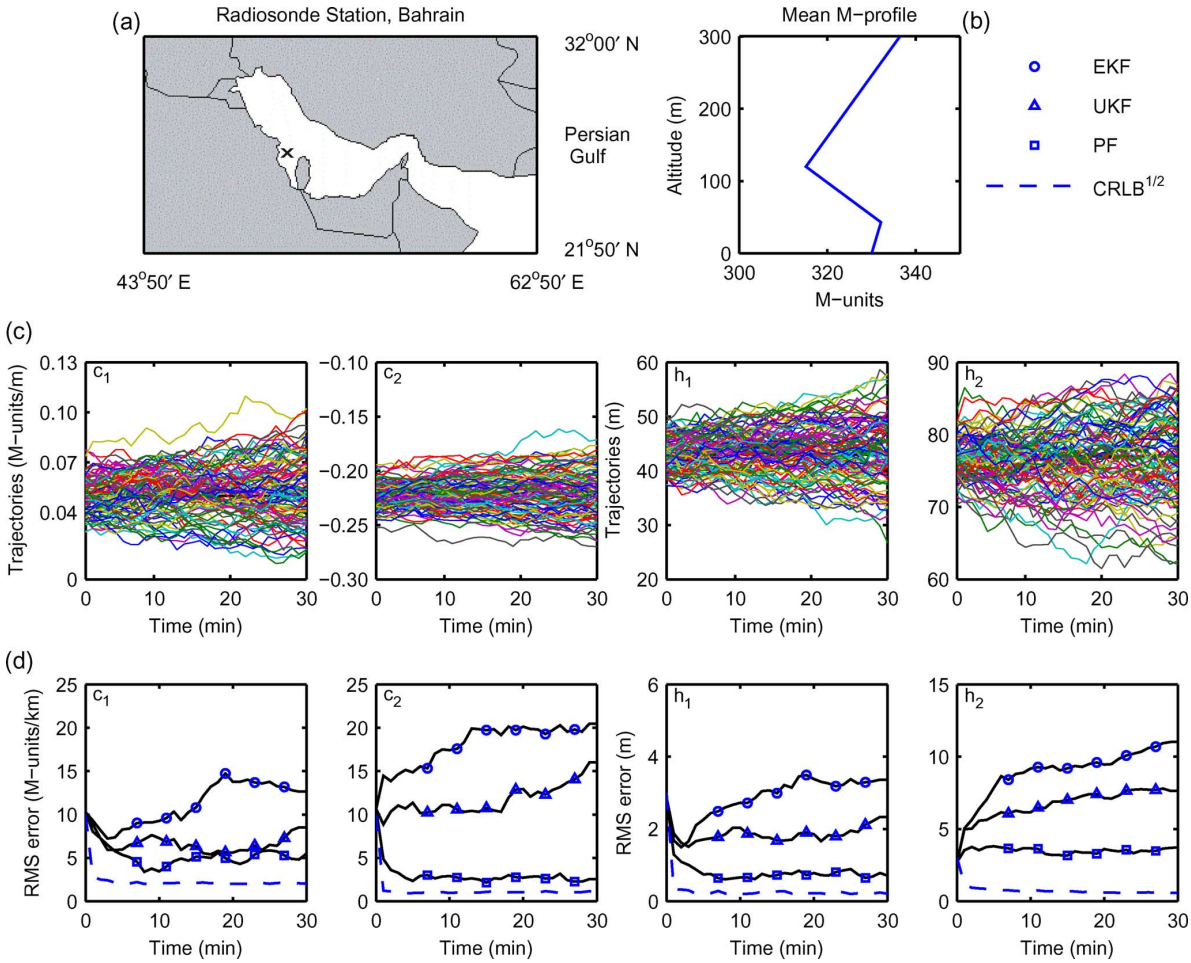

Fig. 1. Case Study I: comparison of the tracking algorithms. (a) Regional map and the location of the station (×), (b) average spring M-profile, (c) evolutions of 100 Monte Carlo trajectories, and (d) RMS errors of the EKF (O), UKF (△), and 200-particle PF (□) obtained from the tracking performance of these trajectories along with the square root of the posterior CRLB (dashed).

TABLE I
CASE STUDY I: COMPARISON OF TRACKING ALGORITHMS AND CRLB
RADIOSONDE STATION BAHRAIN, PERSIAN GULF

Station		**Environment**	
Longitude	50°36′E	Duct Type	Surface-based Duct
Latitude	26°18′N	Month	Mar/Apr/May Average
Elevation	2 m	Time	Day/Night Average
Marsden Square	103	Occurrence	59% Day / 75% Night
Radar		c_1	0.050 M-units/m
Frequency	2.84 GHz	c_2	-0.221 M-units/m
Height	15 m	h_1	43 m
Range Bin	600 m	h_2	77 m
Simulation Parameters			
Monte Carlo Runs	100		
Track Length, k_{max}	30 min – 1 measurement/min		
Initial Covariance	$\mathbf{P}_o$ = diag{(10 M-units/km)^2, (3 m)^2}		
State Noise Covariance	$\mathbf{Q}_k$ = diag{(3 M-units/km)^2, (1 m)^2}		
Measurement Noise	$\mathbf{R}_k$ = diag{(5 dB)^2}, log-normal RCS		

(Fig. 1). The station, average environment, radar and simulation parameters are given in Table I. The state vector $\mathbf{x}$ has four parameters representing the layer thicknesses and slopes of the range-independent SBD M-profile as defined in Appendix A. The layer slopes are given in M-units/m while the RMS errors and standard deviations in the slope estimates are given in M-units/km. The fact that the SBD (excluding evaporative and elevated ducts) is present 67% of the time makes the estimation and tracking of these atmospheric ducts a high priority in the Persian Gulf. The same frequency as that of the Space Range Radar (SPANDAR) [7], [26] is used. The height is set to 15 m, a typical value for a naval radar. New clutter data is provided every minute ($\Delta k = 1$ min) and an overall track length of 30 min is used. The log-normal sea clutter is assumed to have a standard deviation of 5 dB [15]. The values of $\mathbf{Q}_k$, $\mathbf{P}_o$, $\mathbf{R}_k$ are selected in accordance with the values obtained in Appendix B.

The CRLB and the filter performances are calculated using Monte Carlo analysis. First, 100 environmental parameter trajectories are created from the state equation (1) with starting values randomly selected from the prior density taken as a Gaussian as given in Table I. Then, $\mathbf{D}_{k-1}^{22}$ in (9) is calculated using

$$\mathbf{D}_{k-1}^{22} = \mathbf{Q}_{k-1}^{-1} + \frac{1}{N_{\mathrm{MC}}} \sum_{j=1}^{N_{\mathrm{MC}}} \nabla \mathbf{h}\left(\mathbf{x}_k^j\right) \mathbf{R}_k^{-1} \left[\nabla \mathbf{h}\left(\mathbf{x}_k^j\right)\right]^T. \tag{12}$$

TABLE II
PERFORMANCE COMPARISON FOR CASE STUDY I

Method	RMS Error After 30 min.						RTAMS				Average % Improvement Over EKF
	c_1	c_2	h_1	h_2	Avg. Error	Average	c_1	c_2	h_1	h_2	
	(M-units/km)		(m)		(%)	η (%)	(M-units/km)		(m)		
EKF	12.7	20.5	3.36	11.01	14.2	8	11.7	18.8	3.03	9.48	-
UKF	8.5	16.0	2.33	7.64	9.9	12	6.5	11.9	1.87	6.98	36
PF−200	5.5	2.6	0.71	3.72	4.7	30	4.9	2.7	0.73	3.50	71
PF−1000	3.1	1.9	0.38	0.97	2.3	58	3.6	2.2	0.59	1.96	79
PF−5000	2.0	1.7	0.23	0.96	1.6	77	2.9	2.2	0.46	1.20	84
$\sqrt{\mathbf{CRLB}}$	2.0	1.0	0.21	0.57	1.4	100	2.1	1.0	0.24	0.67	90

Each of these 100 environmental trajectories also is tracked using the EKF, UKF and PF. The results are given in Fig. 1 and Table II. The performance metrics are

$$\eta_k(i) = \mathbf{J}_k^{-1/2}(i,i)/\mathrm{RMS}_k(i) \tag{13}$$

$$\mathrm{RTAMS}(i) = \left[\sum_{k=k_1}^{k_2}\sum_{j=1}^{N_{\mathrm{MC}}} \frac{\left(\hat{\mathbf{x}}_k^j(i) - \mathbf{x}_k^j(i)\right)^2}{(k_2-k_1+1)N_{\mathrm{MC}}}\right]^{1/2} \tag{14}$$

$$Improv. = \frac{RTAMS_{\mathrm{EKF}} - RTAMS_{\mathrm{filter}}}{RTAMS_{\mathrm{EKF}}} \tag{15}$$

where $\mathbf{x}_k^j(i)$ is the ith parameter of the true state vector $\mathbf{x}$ at time index k for the jth MC run, RMS_k and η_k are the root mean square error and the filter efficiency at step k, RTAMS is the root time averaged mean square error [21] calculated for the interval $[k_1, k_2]$, and (15) is used to calculate the performance improvement of a filter with respect to the EKF. RTAMS is calculated for the 5–30 min interval so that the initial variation will not affect the performance calculations.

The results in Fig. 1 show that Kalman filters suffer due to their inherent approximations. The measurement equation is highly nonlinear for most of the state space and linearization (EKF) clearly does not work. Since the UKF does not assume linearity, it enjoys an average of 36% improvement over the EKF results. However, a pure Gaussian assumption and high nonlinearity also results in poor UKF estimates with only 12% efficiency. All the particle filters used in this case perform better than both of the Kalman filters. The PF with 5000 particles has an average error of only 1.6%, very close to the value of 1.4% predicted by the CRLB. It is 77% efficient and enjoys a 84% improvement over the EKF.

The EKF uses eight forward model runs $(2 \times n_{\mathrm{x}})$ at each step to compute the Jacobians needed for linearization, whereas the UKF requires nine sigma points $(2 \times n_{\mathrm{x}} + 1)$. Hence, the PF-200, 1000, and 5000 requires a factor of 22, 111, and 556 more CPU time than that of the UKF respectively for this scenario. Hence, the PF is a costly alternative and as a general rule should be avoided as long as the Kalman framework provides reasonable tracking. However, atmospheric parameters sometimes fluctuate abruptly. This requires increasing $\mathbf{Q}_k$ to compensate for the sudden jumps. Initial tests showed that the Kalman structures are more sensitive to these sudden moves and diverge if the sudden jump is large, even after $\mathbf{Q}_k$ is increased, whereas particle filters showed more robust tracking performance. Therefore, it can be concluded that the SBD tracking requires a particle filter approach even though they are computationally expensive.

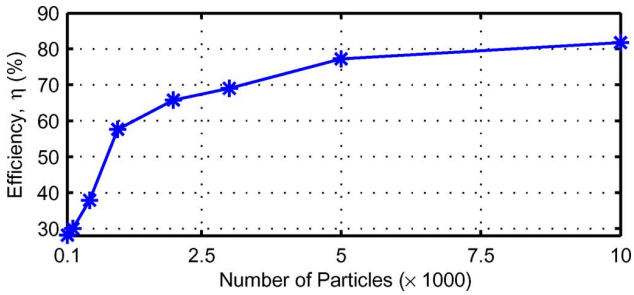

Fig. 2. Case Study I: efficiency of the PF as a function of the number of particles.

Although the results in Table II show the most frequently encountered scenario in the SBD tracking, the simulations show that there are three different cases depending on where you are in the state space. The other two are when the PF and the UKF works but not the EKF and when all three filters perform well. However, these are relatively rare cases and occur only when the nonlinearity is not strong.

An important issue with the particle filters is the selection of the number of particles N_{p} to be used at each step. The increase in the efficiency of the PF with increasing N_{p} is given in Fig. 2 for this case study. Unfortunately, it is hard to determine an optimum value since this curve is scenario dependent. A tropospheric propagation code such as the Terrain Parabolic Equation Model (TPEM) [27] can simulate typically 20 environments per second on a 3 GHz computer. Therefore, for a filter with a 1 min update rate, $N_p < 20 \times 60 = 1200$ can be selected, which corresponds to an average 2% error in the tracked parameters for this scenario. An alternative to this is assuming a discrete state space instead of the continuous one used in this work. Hence, only a finite number of possible environment states needs to be pre-computed so that a larger number of particles can be used. Due to its discrete nature, the problem now can be solved using the grid-based methods such as a hidden Markov model (HMM) based tracking filter which employs a Viterbi algorithm. RFC estimation for a fixed path based on the Viterbi algorithm has been proposed in [12]. However, this requires a sufficiently dense gridding of the state space, which very quickly will grow as the state dimension increases.

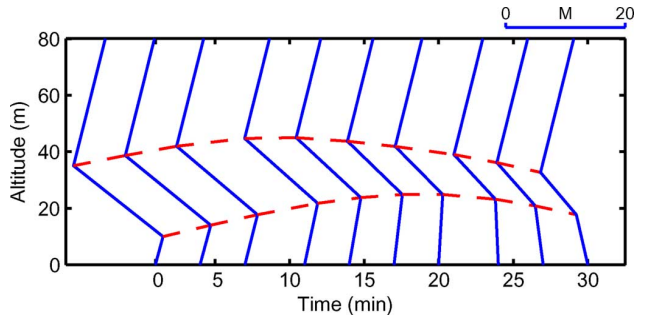

Fig. 3. Case Study II: temporal evolution of the range-independent duct.

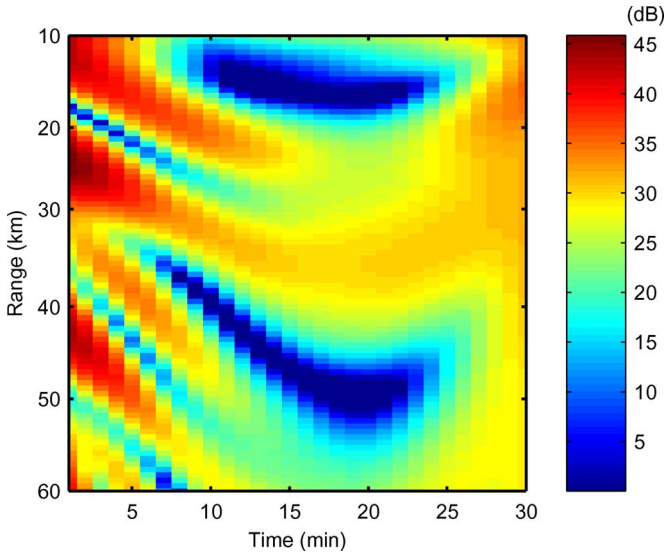

Fig. 4. Case Study II: evolution of the highly nonlinear relative radar clutter $\mathbf{y}_k$ (decibels) computed for the true environment without $\mathbf{w}_k$.

B. Case Study II: Divergence in Surface-Based Duct Tracking

This example studies the divergence problem in SBD tracking. The height and slope values (Fig. 3) and their variations are selected similar to the helicopter measured real M-profiles obtained in the Wallops'98 experiment [7] (Appendix B). All the radar and simulation parameters are kept the same as Case Study I except $\mathbf{Q}_k$ for the layer slopes and $\mathbf{R}_k$ are taken as $(10\ \mathrm{M-units/km})^2$ and $(4\ \mathrm{dB})^2$, respectively. This trajectory is tracked 100 times by each filter to obtain divergent track probabilities.

The evolution of the clutter signal without the addition of noise is given in Fig. 4. The strong nonlinearity of $\mathbf{h}(\mathbf{x}_k)$ results in a high percentage of track divergence for the Kalman filters. For this case, a track is declared as divergent if any of the slope estimates for c_1 or c_2 have a RMS error greater than 50 M-units/km or any of the layer thickness estimates for h_1 or h_2 have a RMS error larger than 5 m for any 5 consecutive minutes. A typical track result is given in Fig. 5 for each filter type. The divergence statistics of the filters are provided in Table III. Similar to Case Study I, the PF performs significantly better than both the Kalman filters and the UKF is better than the EKF. Both Kalman filters mostly were able to follow the thickness variations but failed in tracking the slopes which usually have more effect on the clutter return. Interestingly, the EKF RTAMS

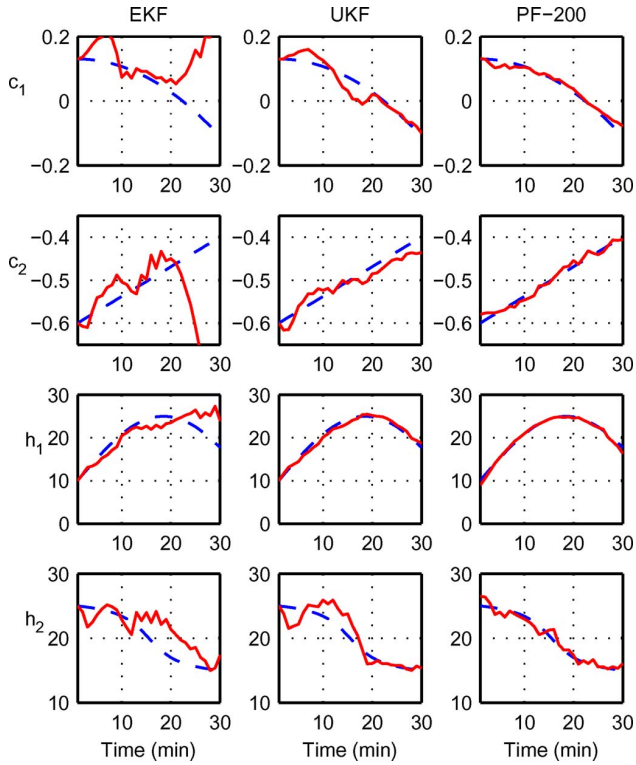

Fig. 5. Case Study II: temporal tracking of the range-independent SBD. c_1 and c_2 are in M-units/m and h_1 and h_2 are in meters. True trajectories (dashed) and filter estimates (solid) for the EKF, UKF, and PF-200.

TABLE III
PERFORMANCE COMPARISON FOR CASE STUDY II

Method	Average RTAMS		Divergent Track Percentage After		
	M-units/km	m	10 min.	20 min.	30 min.
EKF	84.2	2.9	47	69	90
UKF	41.8	3.3	0	29	37
PF−200	27.7	0.9	0	0	17
PF−1000	16.2	0.5	0	0	2

error for the layer thickness is less than that of the UKF. However, this is more than offset by the fact that after only 10 min, the EKF reached a 47% divergence rate while none of the UKF runs diverged. The PF-200 starts to diverge after 30 min with a 17% rate and only 2% of the PF-1000 runs failed to track the duct after 30 min.

C. Case Study III: Range-Dependent Evaporation Duct Tracking in Coastal Regions

This example compares the tracking performances of the three filters in an evaporation duct environment. Evaporation duct differs significantly from the SBD in terms of the nonlinearity of the measurement equation (2). The clutter in an evaporation duct environment does not have the complex patterns of the SBD-induced clutter such as the one in Fig. 4. Except for the very thick ducts which rarely occur, the evaporative duct clutter decreases monotonically with range and the nonlinearities are small [6]. This means that the Kalman filters will no longer suffer from the nonlinearities which severely limited their usage in the previous SBD tracking examples.

TABLE IV
CASE STUDY III: COASTAL RANGE-DEPENDENT EVAPORATION DUCT TRACKING, EASTERN MEDITERRANEAN

Region		**Radar**	
Longitude	20^oE-30^oE	Frequency	5 GHz
Latitude	30^oN-40^oN	Height	15 m
Marsden Square	142	Range Bin	100 m
Environment			
Duct Type		Range-Dependent Evaporation Duct	
Month/Time		July/Day Time Average	
Mean Duct Height		16.4 m	
% Time EDH>10 m		81.7%	
% Time Air-Sea $\triangle T < 1^oC$		87.2%	
Simulation Parameters			
Track Length, k_{max}		120 min – 1 measurement/2 min	
Initial Covariance		$\mathbf{P}_o$ = diag{(3 m)^2}	
State Noise Covariance		$\mathbf{Q}_k$ = diag{(0.707 m)^2}	
Measurement Noise		$\mathbf{R}_k$ = diag{(3 dB)^2}, log-normal RCS	

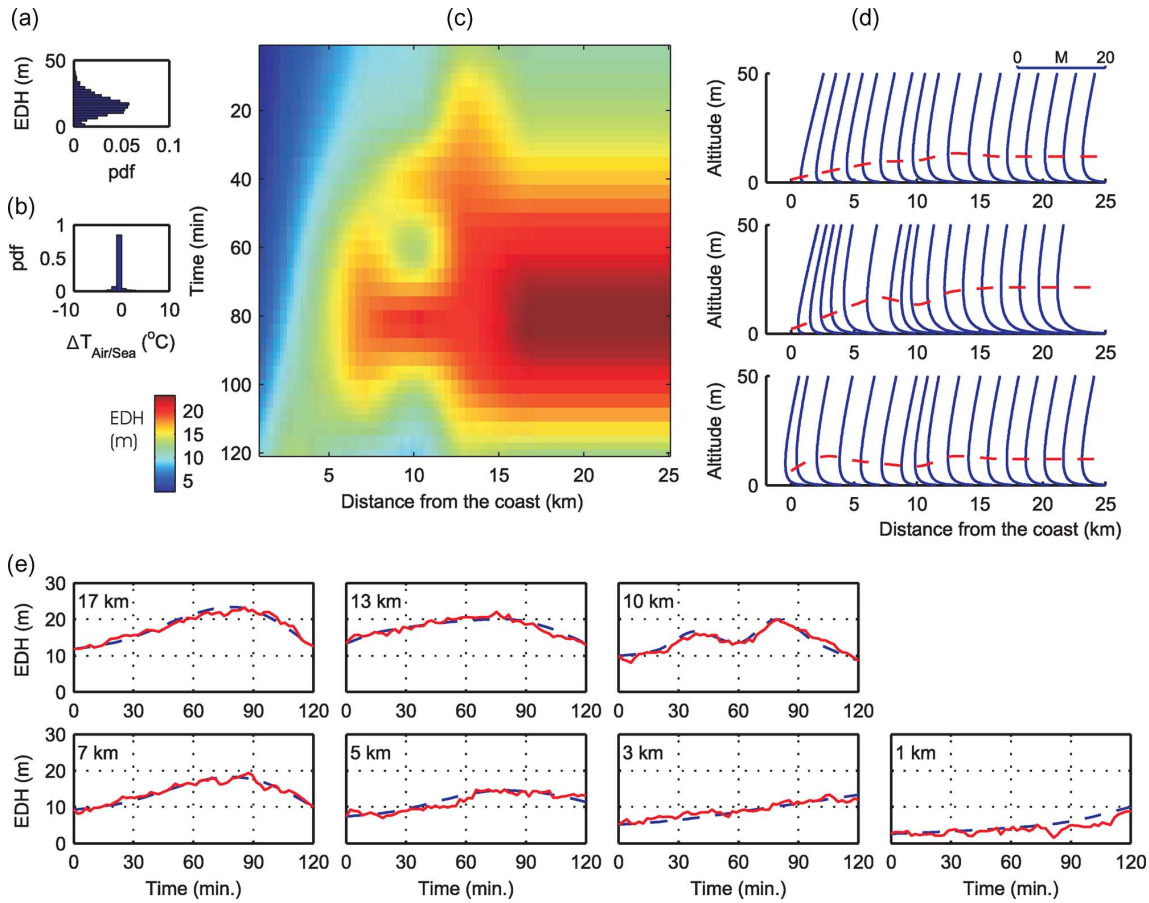

Fig. 6. Case Study III: range-dependent evaporation duct tracking. (a) Evaporation duct height (EDH) statistics and (b) air-sea temperature difference statistics for the given region/month/time, (c) spatio-temporal evolution of the simulated EDH, (d) 2-D M-profiles at 0, 60, and 120 min, and (e) the evolution of EDH for the selected range grid that is used to construct the state vector $\mathbf{x}_k$ (dashed line as the true value, solid line as the EKF track).

Eastern Mediterranean is selected for this example. Day time statistics of July are used. A summary of the selected region, environmental conditions, radar and simulation parameters are given in Table IV. The naval radar is taken to be located at 25 km, looking towards the shore. It should be noted that evaporation ducts thicker than 10 m exist more than 80% of the time in this region. The regional statistics are again taken from the environmental library of AREPS [25]. The regional evaporation duct height (EDH) pdf is given in Fig. 6(a) together with the pdf for the air-sea temperature difference in Fig. 6(b). The small temperature difference makes possible the representation of the vertical evaporative M-profile using only the EDH [28] as given in Appendix A.

A complex, temporally evolving, range-dependent coastal evaporation duct as given in Fig. 6(c) is artificially created in accordance with the regional EDH pdf. Corresponding 2-D

TABLE V
PERFORMANCE COMPARISON FOR CASE STUDY III

Method	Average RMS Error 1 hr. (m)	Average RMS Error 2 hr. (m)	Average RTAMS (m)	Avg. % Improv. Over EKF
EKF	1.17	0.88	1.08	-
UKF	1.17	0.90	1.07	1
PF−200	1.19	1.93	1.38	–29
PF−1000	1.13	1.42	1.13	–6

M-profiles at $\mathrm{t} = 0$, 60, and 120 min are shown in Fig. 6(d). As a typical coastal duct, it has high variability near the coastal zones with multiple local disturbances with 10–30 min and 2–10 km scales similar to those measured in [29]–[31], while it gets more uniform as the distance from the shore increases. It also includes the formation and dissipation of a strong offshore evaporative duct (between 60–100 min) and as usual, the duct starts to lose its strength as it gets closer to the land. To better represent the coastal zones, a denser grid is used for these regions. The nonuniform grid used here has seven ranges at 1, 3, 5, 7, 10, 13, and 17 km from the shore. Hence, the state vector is composed of the EDH at these seven ranges (Appendix A).

The tracking performance of the EKF, UKF, PF-200, and PF-1000 are given in Table V. A typical EKF track is provided in Fig. 6(e). Both Kalman filters have a high performance with an average RTAMS of around 1 m. Since the nonlinearity is not severe, the 1st order accurate linearization used by the EKF is as good as the higher order accurate UKF and overall, the UKF achieves only 1% improvement over the EKF. Unlike the SBD tracking, the 200 point PF is no match for the Kalman filters, while PF-1000 is now comparable to the EKF.

The results show that Kalman filters are able to track evaporative ducts successfully, and can only be outperformed by a very high N_{P} PF which is computationally much more expensive.

D. Case Study IV: Wallops'98 Experiment

The last example is the spatial tracking of the surface-based duct observed during the Wallops'98 experiment. The regional, environmental and radar system parameters are given in Table VI. For the sake of simplicity, a range-independent M-profile is used and its evolution with the changing azimuth is tracked. Hence, the state vector $\mathbf{x}_k$ has only four parameters representing the layer thicknesses and slopes of the range-independent SBD M-profile as defined in Appendix A. The step index k represents the evolving azimuth of the rotating radar. SPANDAR is a high gain antenna with a beamwidth of 0.39°. Therefore, the step size can be on the order of 1° or less.

The evolution of the clutter with changing azimuth is given in the plan position indicator (PPI) map in Fig. 7(a). Since Wallops data is coastal, the spatial variability observed in the plot is expected to be more than a typical non-littoral marine environment. Clutter maps evolving faster or slower than the selected one have been observed throughout the experiment. The region 90°–170° is selected for tracking [Fig. 7(b)]. Tracking is initiated at 90° using the maximum a posteriori (MAP) solution obtained from the genetic algorithms (GA) inversion [7] result at that azimuth. Then a 100-point PF is used to track the environment as SPANDAR rotates between 90 and 170°.

TABLE VI
CASE STUDY IV: RANGE-INDEPENDENT SURFACE-BASED DUCT TRACKING, WALLOPS'98

Region		**Radar**	
Name	Wallops VA	Name	Space Range Radar
Longitude	75.48^{o}W	Frequency	2.84 GHz
Latitude	37.83^{o}N	Height	30.78 m
Marsden Square	116	Range Bin	600 m
Environment			
Duct Type		Range-Independent SBD	
Date (Clutter Map)		14:00 EST, 2 April 1998 (Map 18)	
Region of Interest		90–170°, 10–60 km	
Helicopter Measurement		150°, 10–60 km	

The Kalman filters perform poorly and diverge quickly, similar to the first two cases where surface-based ducts were tracked. Therefore only the results of a 100-point PF tracking are given in Fig. 8.

Unfortunately the helicopter measurements (Appendix B) are only available for 150°. Hence, this azimuth is used to compare different techniques. For comparison purposes, the range-independent profile at 150° azimuth is also inverted using GA. A typical GA run for a given azimuth requires 10,000 forward model (split-step FFT parabolic equation) calculations. The tracking filter uses far fewer samples (e.g., 10,000 versus 100) to achieve a performance similar to that of an individual GA inversion at a given azimuth angle. This is due to the fact that the PF uses not only the clutter measurement at that azimuth but the measurements and environmental information from the previous azimuths as well. Note that, even though the estimated individual layer thicknesses are different, the overall duct height is well determined both in the PF and the GA results.

Finally, the M-profiles and the clutter structures of the PF and GA solutions, and the helicopter measurements are given in Fig. 9 along with the coverage diagram one would obtain from an environment given by the PF result at 150°. The mean helicopter profile (HP) is the average profile one would obtain from the range-dependent helicopter measurement. Both algorithms provide an M-profile close to that of the mean HP [see Fig. 9(a)] and similar clutter returns [see Fig. 9(c)].

IV. DISCUSSION

A fundamental question for a real RFC tracking system is the temporal/spatial step size. The continuous real-time inflow of clutter data enables RFC techniques to capture much finer details in the local environmental conditions. Track updates at every minute or two seems to be a reasonable choice for tracking since the typical RMS error in the propagation factor has been shown to exceed 6 dB after 30 min due to temporal decorrelation of the environmental parameters [32]. Tracking faster may necessitate a decrease in the number of particles to be used in the PF which may degrade the track effectiveness.

During the simulations some special cases other than the provided examples have been noted which can cause track divergence. One of these is when one of the layer thickness parameters gets very small for a short period of time. Since the layer

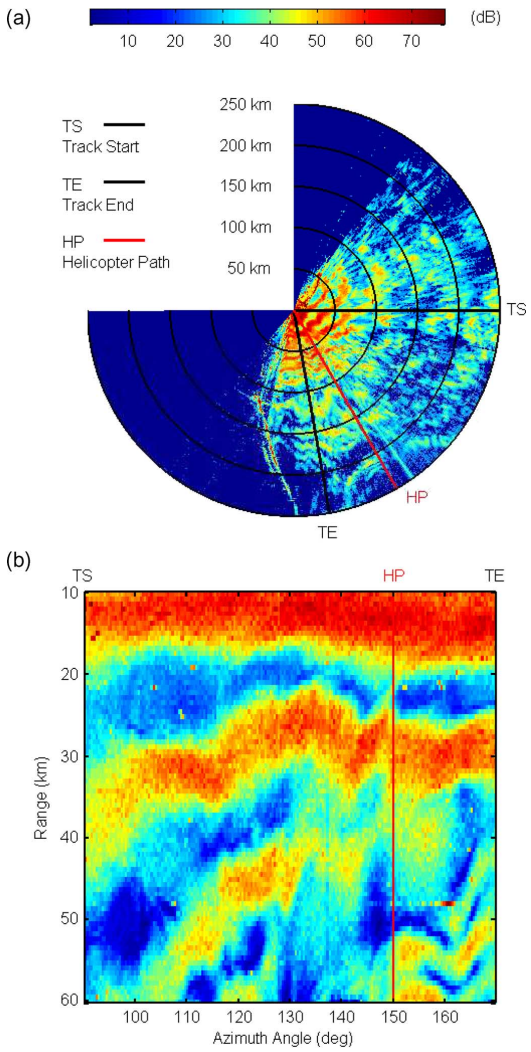

Fig. 7. Case Study IV: (a) PPI image of the radar clutter $\mathbf{y}_k$ measured by SPANDAR during the Wallops'98 experiment (Map 18, April, 2007) and (b) the evolution of the clutter within the region of interest.

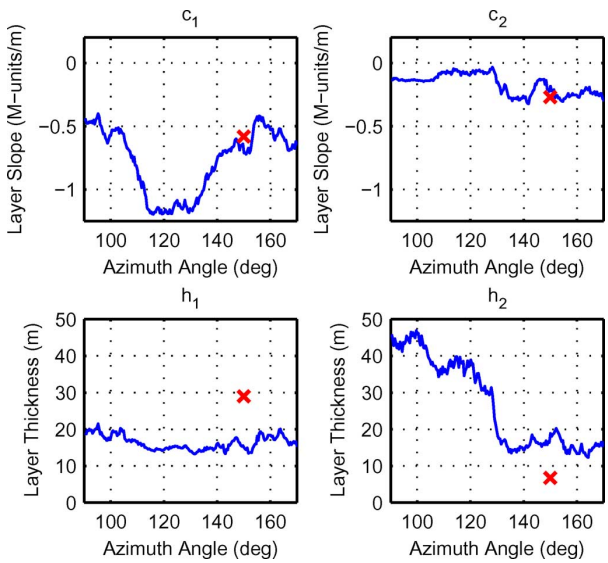

Fig. 8. Case Study IV: range-independent surface-based duct tracking results obtained using the SPANDAR clutter map by a 100-point PF. The results of the GA inversion performed at 150° is shown by cross.

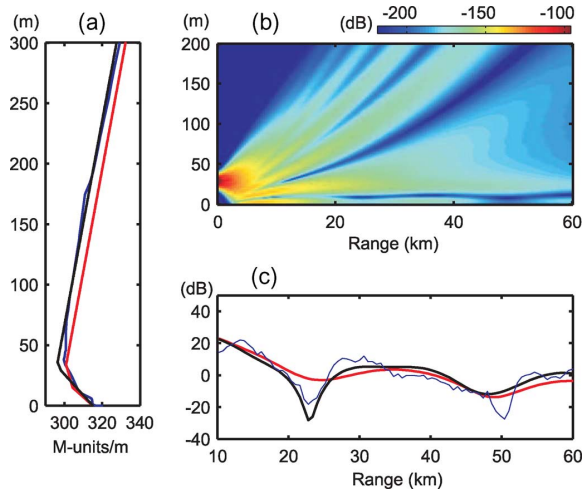

Fig. 9. Case Study IV: tracking results. (a) M-profile estimates of the PF tracking (red) and the GA (black) plotted together with the mean helicopter profile (blue) at 150°, (b) coverage diagram for the PF solution, and (c) the relative clutter power given by the three M-profiles in (a).

is thin it has minimal effect on electromagnetic propagation so the slope of this layer does not have any significance on the overall clutter structure. This leads to major deviations in the slope parameter and when the layer starts to thicken again, the track diverges since the starting slope value is too far from the true one. The PF is more resilient to this type of divergence than the Kalman filters.

The second case is when the duct height becomes less than the antenna height for some range interval (in a range-dependent profile) even for a short duration. Since the source now is outside the waveguide, the sea clutter drops possibly resulting in track divergence.

The final case is when the duct becomes very strong for some range interval (in a range-dependent profile) even for a short duration. A strong duct is formed when the inversion slope is so strong (highly negative) that the entire electromagnetic field is trapped before it reaches the upper boundary of the inversion layer. Then any inversion layer thickness value larger than this total entrapment thickness will have the same effect on the clutter, resulting in large deviations in the inversion layer thickness and as the duct loses its strength, divergence occurs since the starting value of the inversion layer thickness is too far from its true value.

V. Conclusion

The extended and unscented Kalman and particle filters have been studied for tracking the spatial and temporal evolution of the lower atmospheric index of refraction using the radar clutter return. The divergence statistics, computational complexities, and tracking performances of these filters were compared to each other using the posterior Cramér-Rao lower bound through four case studies. The results showed that the clutter can be a rich source of information for real-time tracking of the 3-D environment in which the radar is operating.

The Kalman filters showed that they can be used successfully only for the evaporative duct tracking but were limited by the nonlinearity of the mapping from environmental refractivity to clutter (that uses the split step fast Fourier transform parabolic equation) and the non-Gaussianity of the environmental parameter densities, especially for the surface-based duct tracking. In contrast, the particle filter showed that it can successfully track all four of the cases although it required much larger computation times relative to the Kalman filters.

Appendix A
Creation of the 2-D Modified Refractivity Profile From State Variables

Surface-based ducts (SBD) are represented by the commonly used tri-linear M-profiles. Each tri-linear profile requires four parameters: slope and thickness of the base (c_1, h_1) and inversion layers (c_2, h_2). The top layer slope is taken to be constant at 0.118 M-units/m. For range-dependent profiles, the M-profile parameters are defined at $n_{\rm r}$ range intervals and the values at other ranges are calculated using a cubic fit. Hence, the number of state parameters $n_{\rm x} = 4n_{\rm r}$. The 2-D M-profile is calculated using the following procedure:

$$\mathbf{x}_k = \left[\mathbf{m}_1^T\ \mathbf{m}_2^T\ \ldots\ \mathbf{m}_{n_{\rm r}}^T\right]^T \tag{A.16}$$

$$\mathbf{m}_i = \left[c_1(r_i) c_2(r_i) h_1(r_i) h_2(r_i)\right]^T,\ \ i = 1, \ldots, n_{\rm r} \tag{A.17}$$

$$M(z,r) = M_0 + \begin{cases} \tilde{c}_1 z & \text{if } z \le \tilde{h}_1 \\ \tilde{c}_1 \tilde{h}_1 + \tilde{c}_2 (z - \tilde{h}_1) & \text{if } \tilde{h}_1 \le z \le \tilde{h}_2 \\ \tilde{c}_1 \tilde{h}_1 + \tilde{c}_2 \tilde{h}_2 & \text{if } z \ge \tilde{h}_2 \\ +0.118(z - \tilde{h}_1 - \tilde{h}_2), & \end{cases} \tag{A.18}$$

where M_0 is the base refractivity usually taken as 330 {M-units/m}, $\mathbf{m}_i$ represent the trilinear profiles at $n_{\rm r}$ different ranges defined in the state vector, $\tilde{c}_1$, $\tilde{c}_2$, $\tilde{h}_1$, and $\tilde{h}_2$ are parameters obtained by a cubic fit for range r.

Evaporative ducts are represented using only the evaporative duct height, which is true when the air and sea temperatures are almost identical with a neutrally buoyant boundary layer. Range-dependence is similarly achieved by defining the duct height at various ranges and interpolating in between using cubic fit. Hence, the number of state parameters $n_{\rm x} = n_{\rm r}$ for evaporative duct problems. The 2-D evaporative duct is constructed using the log-linear evaporative duct formula given in [33]:

$$\mathbf{x}_k = \left[h_{\rm d}(r_1)\ h_{\rm d}(r_2)\ \ldots\ h_{\rm d}(r_{n_{\rm r}})\right]^T \tag{A.19}$$

$$M(z,r) = M_0 + c_{\rm o}\left(z - \tilde{h}_{\rm d} \ln \frac{z + z_{\rm o}}{z_{\rm o}}\right) \tag{A.20}$$

where $\tilde{h}_{\rm d}$ represents the duct height obtained by a cubic fit at range r, the constant $c_{\rm o}$ and the roughness factor $z_{\rm o}$ are taken as 0.13 and 1.5×10^{-4}, respectively.

State vector for a mixed type range-dependent/independent duct is created using $4 + 1$ (SBD+evaporation) parameters at each of the $n_{\rm r}$ ranges. Then the evaporative M-profile is appended to the bottom of the trilinear SBD profile.

Appendix B
State Equation—Environmental Model

The spatial and temporal evolution of the environmental parameters are taken as a first order autoregressive (AR) process with an exponentially decaying autocorrelation function. This structure is selected after the analysis of the helicopter data collected during the Wallops'98 experiment. A helicopter from John Hopkins University (JHU) measured the 2-D M-profile on a fixed path at 150° azimuth from the Space Range Radar (SPANDAR) several times on April 02, 1998 and these measurements are processed into 10 2-D helicopter profiles. Each helicopter profile takes about 24 minutes to measure and is composed of vertical M-profiles every 1.852 km (1 nautical mile) out to 60 km. Therefore, the variation in the M-profiles unfortunately is a combination of both spatial and temporal fluctuations. The variation in two successive M-profiles in range in any given helicopter profile is assumed to be purely spatial to obtain an approximation to the spatial autocorrelation. In other words, the mean helicopter flight time between successive vertical M-profiles is ignored.

The best trilinear fit for each of these vertical M-profiles is computed (Fig. 10) for each helicopter profile. The autocorrelation for each parameter is calculated using the Yule-Walker method. It also is assumed that these parameters are stationary random processes and hence the spatial autocorrelation only depends on the distance between the two vertical profiles. For the spatial and temporal step sizes used in this paper, the results provided an autocorrelation between 0.97 and 1 for both the layer slopes and thicknesses. The standard deviation for the layer slopes and thicknesses are observed to vary between 5–100 M-units/km and 1-10 m, respectively, for these 10 profiles. However, it should be noted that these values are by no means general. From many previous experiments such as the Variability of Coastal Atmospheric Refractivity (VOCAR) [34], it is known that these values are strong functions of region, season, time of the day and mesoscale atmospheric processes. For example, experiments indicate that Santa Ana-induced (warm and dry offshore winds in Southern and Baja California) SBDs typically have higher spatial variability than the subsidence-induced SBDs [35]. It has been known that duct parameters such as the duct height can stay stable for days, followed by rapid fluctuations [29]. Spatial variability also has challenging and dynamic patterns as shown during the Wallops'2000 experiment [26]. Hence, different environmental models may be necessary for different applications or regions. One solution can be using multiple models created by observing the most common patterns in the region of interest.

Appendix C
Measurement Equation—Propagation Model

The measurement equation provides $\mathbf{y}_k$, the radar clutter power in dB, for an environment described by the state vector $\mathbf{x}_k$. First the field is propagated in range using the following recursive split-step FFT PE formula [27]

$$u_k(z, r + \triangle r) = \exp\left[ik_{\rm o} \triangle r M(\mathbf{x}_k) 10^{-6}\right] \mathfrak{F}^{-1} \times \left\{\exp\left[i \triangle r \left(\sqrt{k_{\rm o}^2 - k_{\rm z}^2} - k_{\rm o}\right)\right] \mathfrak{F}\left\{u_k(z,r)\right\}\right\} \tag{C.21}$$

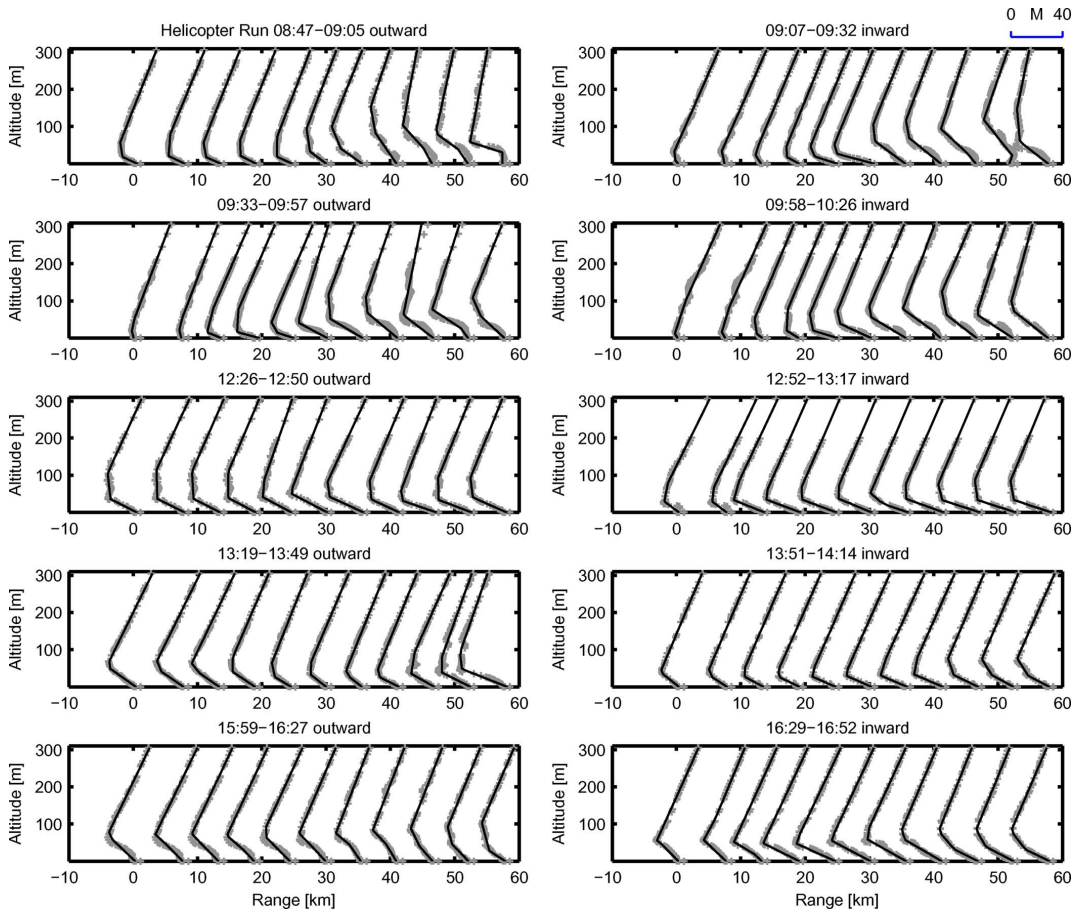

Fig. 10. Ten 2-D M-profiles measured by JHU helicopter, Wallops'98 experiment (gray) and best trilinear profile fit for each measurement (black).

where $u_k(z,r)$ is the vertical electromagnetic field at range r at step index k, $k_{\rm o}$ and $k_{\rm z}$ are the wavenumber and its vertical component, $\triangle r$ is the range increment in PE, $\mathfrak{F}$ and $\mathfrak{F}^{-1}$ are the Fourier and inverse Fourier transforms and $M(\mathbf{x}_k)$ is the 2-D M-profile $M(z,r)$ computed in Appendix A. Following [7], the clutter power $\mathbf{P}_c$ for low grazing angles can be calculated using

$$\mathbf{P_c} = c\mathbf{L}^{-2}(\mathbf{x}_k) r \sigma^{\rm o} \tag{C.22}$$

where c accounts for the constant terms in the radar equation, $\mathbf{L}(\mathbf{x}_k)$ is the one way propagation loss obtained from the electromagnetic field $u_k(z,r)$ calculated at the effective scattering height given as 0.6 times the mean wave height [36] and $\sigma^{\rm o}$ is the normalized sea surface RCS.

The measurement equation (2) can be obtained by representing (C.22) in dB with the following definitions:

$$\mathbf{y}_k = 10\log(\mathbf{P_c}) \quad \mathbf{w}_k = 10\log(\sigma^{\rm o}) \tag{C.23}$$

$$\mathbf{h}(\mathbf{x}_k) = -20\log\mathbf{L}(\mathbf{x}_k) + 10\log(cr) \tag{C.24}$$

where the measurement noise $\mathbf{w}_k$ is additive Gaussian since $\sigma^{\rm o}$ is the sea surface RCS with log-normal pdf. For tracking the environment, there probably will be periods of minutes between two measurements and the quantities above actually will be averaged over the interval, which may reduce the log-normal measurement noise.

APPENDIX D

A. Unscented Kalman Filter Equations

The UKF uses the following recursive formulation where $2n_{\rm x}+1$ sigma points $\{\boldsymbol{\mathcal{X}}^i\}_{i=0}^{2n_{\rm x}}$ and their corresponding weights W^i are generated and used with the unscented transform (UT) to perform the mean $(\widehat{\mathbf{x}}_k)$ and covariance $(\mathbf{P}_k)$ calculations required in the Kalman framework. The UT weights are given in terms of the scaling parameter $\lambda = \alpha^2(n_{\rm x}+\kappa) - n_{\rm x}$ and prior knowledge parameter β where α is used to control the spread of the sigma points around the mean and κ is the secondary scaling parameter. α, β, and κ are taken as 0.1, 2, and 0, respectively.

UT weights and sigma points are generated using

$$\boldsymbol{\mathcal{X}}_{k-1}^0 = \widehat{\mathbf{x}}_{k-1|k-1}$$

$$W_{\rm m}^0 = \frac{\lambda}{n_{\rm x}+\lambda}, \quad W_{\rm cov}^0 = W_{\rm m}^0 + \beta + 1 - \alpha^2 \tag{D.25}$$

$$\boldsymbol{\mathcal{X}}_{k-1}^i = \widehat{\mathbf{x}}_{k-1|k-1} \pm \left(\sqrt{(n_{\rm x}+\kappa)\mathbf{P}_{k-1|k-1}}\right)_i$$

$$W_{\rm m}^i = W_{\rm cov}^i = \frac{0.5}{n_{\rm x}+\lambda} \quad i = 1,2,\ldots,2n_{\rm x} \tag{D.26}$$

where $(\sqrt{\cdot})_i$ is the ith column of the matrix square root. The prediction step is composed of

$$\boldsymbol{\mathcal{X}}^i_{k|k-1} = \mathbf{F}\boldsymbol{\mathcal{X}}^i_{k-1}, \quad \boldsymbol{\mathcal{Y}}^i_{k|k-1} = \mathbf{h}\left(\boldsymbol{\mathcal{X}}^i_{k|k-1}\right) \tag{D.27}$$

$$\widehat{\mathbf{x}}_{k|k-1} = \sum_{i=0}^{2n_{\mathrm{x}}} W^i_{\mathrm{m}} \boldsymbol{\mathcal{X}}^i_{k|k-1}, \quad \widehat{\mathbf{y}}_{k|k-1} = \sum_{i=0}^{2n_{\mathrm{x}}} W^i_{\mathrm{m}} \boldsymbol{\mathcal{Y}}^i_{k|k-1}$$

$$\mathbf{P}_{k|k-1} = \mathbf{Q}_{k-1} + \sum_{i=0}^{2n_{\mathrm{x}}} W^i_{\mathrm{cov}} \left[\boldsymbol{\mathcal{X}}^i_{k|k-1} - \widehat{\mathbf{x}}_{k|k-1}\right] \times \left[\boldsymbol{\mathcal{X}}^i_{k|k-1} - \widehat{\mathbf{x}}_{k|k-1}\right]^T \tag{D.28}$$

and the update step uses

$$\mathbf{P}_{xy} = \sum_{i=0}^{2n_{\mathrm{x}}} W^i_{\mathrm{cov}} \left[\boldsymbol{\mathcal{X}}^i_{k|k-1} - \widehat{\mathbf{x}}_{k|k-1}\right] \left[\boldsymbol{\mathcal{Y}}^i_{k|k-1} - \widehat{\mathbf{y}}_{k|k-1}\right]^T$$

$$\mathbf{P}_{yy} = \sum_{i=0}^{2n_{\mathrm{x}}} W^i_{\mathrm{cov}} \left[\boldsymbol{\mathcal{Y}}^i_{k|k-1} - \widehat{\mathbf{y}}_{k|k-1}\right] \left[\boldsymbol{\mathcal{Y}}^i_{k|k-1} - \widehat{\mathbf{y}}_{k|k-1}\right]^T$$

$$\mathbf{K}_k = \mathbf{P}_{xy}(\mathbf{P}_{yy} + \mathbf{R}_k)^{-1} \tag{D.29}$$

$$\widehat{\mathbf{x}}_{k|k} = \widehat{\mathbf{x}}_{k|k-1} + \mathbf{K}_k(\mathbf{y}_k - \widehat{\mathbf{y}}_{k|k-1}) \tag{D.30}$$

$$\mathbf{P}_{k|k} = \mathbf{P}_{k|k-1} - \mathbf{K}_k(\mathbf{P}_{yy} + \mathbf{R}_k)\mathbf{K}_k^T. \tag{D.31}$$

B. Sequential Importance Resampling Filter Equations

The SIR algorithm [21] uses N particles $\{\boldsymbol{\mathcal{X}}^i\}_{i=1}^N$ to represent the pdf at each step k. The filter has the predict and update sections just as in a KF but the SIR filter will use these sections to propagate the particles instead of mean and covariance calculations.

The initial set of particles $\{\boldsymbol{\mathcal{X}}^i_{\mathrm{o}}\}_{i=1}^N$ are sampled from the prior $\mathrm{p}(\mathbf{x}_{\mathrm{o}})$. The SIR filter uses the importance sampling density as the transitional prior $\mathrm{p}(\mathbf{x}_k|\mathbf{x}_{k-1})$. Therefore, the prediction step consists of sampling from this pdf. Then the normalized weight W^i_k of each particle is calculated from its likelihood function. The update step includes the resampling section where a new set of N particles is generated from the parent set according to the weights of the parent particles. Hence, a single iteration of the recursive SIR algorithm can be summarized as

$$\left\{\boldsymbol{\mathcal{X}}^i_{k|k-1}\right\}_{i=1}^N \sim \mathrm{p}(\mathbf{x}_k|\mathbf{x}_{k-1}) \tag{D.32}$$

$$W^i_k = \frac{\mathrm{p}\left(\mathbf{y}_k|\boldsymbol{\mathcal{X}}^i_{k|k-1}\right)}{\sum_{i=1}^N \mathrm{p}\left(\mathbf{y}_k|\boldsymbol{\mathcal{X}}^i_{k|k-1}\right)} \tag{D.33}$$

$$\left\{\boldsymbol{\mathcal{X}}^i_{k|k}\right\}_{i=1}^N = \mathrm{Resample}\left[W^j_k, \left\{\boldsymbol{\mathcal{X}}^j_{k|k-1}\right\}_{j=1}^N\right]$$

$$s.t.\ \ \mathrm{Pr}\left\{\boldsymbol{\mathcal{X}}^i_{k|k} = \boldsymbol{\mathcal{X}}^j_{k|k-1}\right\} = W^j_k \tag{D.34}$$

ACKNOWLEDGMENT

The authors would like to thank T. Rogers at SPAWAR, San Diego, CA, for providing the Wallops'98 clutter maps and providing insight on COAMPS and atmospheric modeling and the Applied Physics Laboratory, John Hopkins University, Baltimore, MD, for providing the helicopter refractivity measurements.

REFERENCES

[1] J. R. Rowland and S. M. Babin, "Fine-scale measurements of microwave profiles with helicopter and low cost rocket probes," *Johns Hopkins APL Tech. Dig.*, vol. 8, no. 4, pp. 413–417, 1987.

[2] E. R. Thews, "Timely prediction of low-altitude radar performance in operational environments using *in situ* atmospheric refractivity data," *Proc. Inst. Elect. Eng.*, vol. 137, no. F-2, pp. 89–94, 1990.

[3] R. M. Hodur, "The naval research laboratory's coupled ocean/atmosphere mesoscale prediction system (COAMPS)," *Monthly Weather Rev.*, vol. 125, no. 7, pp. 1414–1430, 1996.

[4] A. Willitsford and C. R. Philbrick, "Lidar description of the evaporative duct in ocean environments," in *Proc. SPIE*, Bellingham, WA, Sep. 2005, vol. 5885.

[5] A. R. Lowry, C. Rocken, S. V. Sokolovskiy, and K. D. Anderson, "Vertical profiling of atmospheric refractivity from ground-based GPS," *Radio Sci.*, vol. 37, no. 3, pp. 1041–1059, 2002, 10.1029/2000RS002565.

[6] L. T. Rogers, C. P. Hattan, and J. K. Stapleton, "Estimating evaporation duct heights from radar sea echo," *Radio Sci.*, vol. 35, no. 4, pp. 955–966, 2000, 10.1029/1999RS002275.

[7] P. Gerstoft, L. T. Rogers, J. Krolik, and W. S. Hodgkiss, "Inversion for refractivity parameters from radar sea clutter," *Radio Sci.*, vol. 38, no. 3, pp. 1–22, 2003, 10.1029/2002RS002640.

[8] P. Gerstoft, W. S. Hodgkiss, L. T. Rogers, and M. Jablecki, "Probability distribution of low altitude propagation loss from radar sea-clutter data," *Radio Sci.*, vol. 39, pp. 1–9, 2004, 10.1029/2004RS003077.

[9] A. Barrios, "Estimation of surface-based duct parameters from surface clutter using a ray trace approach," *Radio Sci.*, vol. 39 RS6013, pp. 1–15, 2004, 10.1029/2003RS002930.

[10] L. T. Rogers, M. Jablecki, and P. Gerstoft, "Posterior distributions of a statistic of propagation loss inferred from radar sea clutter," *Radio Sci.*, vol. 40, no. 6, pp. 1–14, 2005, 10.1029/2004RS003112.

[11] C. Yardim, P. Gerstoft, and W. S. Hodgkiss, "Estimation of radio refractivity from radar clutter using Bayesian Monte Carlo analysis," *IEEE Trans. Antennas Propag.*, vol. 54, no. 4, pp. 1318–1327, 2006.

[12] S. Vasudevan, R. Anderson, S. Kraut, P. Gerstoft, L. Rogers, and J. Krolik, "Recursive Bayesian electromagnetic refractivity estimation from radar sea clutter," *Radio Sci.*, vol. 42, pp. 1–19, 2007, 10.1029/2005RS003423.

[13] C. Yardim, P. Gerstoft, and W. S. Hodgkiss, "Statistical maritime radar duct estimation using a hybrid genetic algorithm—Markov chain Monte Carlo method," *Radio Sci.*, vol. 42, 2007, 10.1029/2006RS003561.

[14] M. Levy, *Parabolic Equation Methods for Electromagnetic Wave Propagation*. London, U.K.: Institution of Electrical Engineers, 2000.

[15] D. A. Shnidman, "Comparison of low angle radar clutter models," *IEEE Trans. Aerosp. Electron. Syst.*, vol. 41, no. 2, pp. 736–746, 2005.

[16] S. M. Kay, *Fundamentals of Statistical Signal Processing—Volume I: Estimation Theory*. Englewood Cliffs, NJ: Prentice-Hall, 1993.

[17] S. Julier, J. Uhlmann, and H. F. Durrant-White, "A new method for nonlinear transformation of means and covariances in filters and estimators," *IEEE Trans. Autom. Control*, vol. 45, pp. 477–482, 2000.

[18] E. A. Wan and R. van der Merve, "The unscented Kalman filter," in *Kalman Filtering and Neural Networks*, S. Haykin, Ed. New York: Wiley, 2001.

[19] A. Doucet, N. de Freitas, and N. Gordon, *Sequential Monte Carlo Methods in Practice*. New York: Springer, 2001.

[20] B. Ristic, S. Arulampalam, and N. Gordon, *Beyond the Kalman Filter, Particle Filters for Tracking Applications*. Boston, MA: Artech House, 2004.

[21] N. J. Gordon, D. J. Salmond, and A. F. M. Smith, "Novel approach to nonlinear/non-Gaussian Bayesian state estimation," *Proc. Inst. Elect. Eng.*, vol. 140, no. 2, pt. F, pp. 107–113, 1993.

[22] H. L. van Trees, *Detection, Estimation and Modulation Theory*. New York: Wiley, 1968.

[23] P. Tichavský, C. H. Muravchik, and A. Nehorai, "Posterior Cramér-Rao bounds for discrete-time nonlinear filtering," *IEEE Trans. Signal Processing*, vol. 46, no. 5, pp. 1386–1396, 1998.

[24] *"User's Manual for Advanced Refractive Effect Prediction System"* 3rd ed. Space and Naval Warfare Systems Center, Atmospheric Propagation Branch, San Diego, CA, Apr. 2005 [Online]. Available: http://www.spawar.navy.mil/sti/publications

[25] J. K. Stapleton, V. R. Wiss, and R. E. Marshall, "Measured anomalous radar propagation and ocean backscatter in the Virginia coastal region," presented at the 31st Int. Conf. on Radar Meteorology Seattle, WA, Aug. 6–12, 2003.

[26] A. E. Barrios, "A terrain parabolic equation model for propagation in the troposphere," *IEEE Trans. Antennas Propag.*, vol. 42, no. 1, pp. 90–98, 1994.

[27] E. E. Gossard and R. G. Strauch, *Radar Observations of Clear Air and Clouds*. New York: Elsevier, 1983.

[28] I. M. Brooks, A. K. Goroch, and D. P. Rogers, "Observations of strong suface radar ducts over the Persian gulf," *J. Appl. Meteorol.*, vol. 38, pp. 1293–1310, 1999.

[29] B. W. Atkinson, J.-G. Li, and R. S. Plant, "Numerical modeling of the propagation environment in the atmosphere boundary layer over the Persian gulf," *J. Appl. Meteorol.*, vol. 40, pp. 586–602, 2001.

[30] B. W. Atkinson and M. Zhu, "Radar-duct and boundary-layer characteristics over the area of The Gulf," *Q. J. R. Meteorol. Soc.*, vol. 131, pp. 1923–1953, 2005.

[31] L. T. Rogers, "Effects of variability of atmospheric refractivity on propagation estimates," *IEEE Trans. Antennas Propag.*, vol. 44, no. 4, pp. 460–465, 1996.

[32] R. A. Paulus, "Evaporation duct effects on sea clutter," *IEEE Trans. Antennas Propag.*, vol. 38, no. 11, pp. 1765–1771, 1990.

[33] T. Haack and S. D. Burk, "Summertime marine refractivity conditions along coastal California," *J. Appl. Meteorol.*, vol. 40, pp. 673–687, 2001.

[34] R. A. Paulus, "An overview of an intensive observation period on variability of coastal atmospheric refractivity," in *AGARD/NATO Conf. on Propagation Assessment in Coastal Environments*, Bremerhaven, Germany, Feb. 1995.

[35] J. P. Reilly and G. D. Dockery, "Influence of evaporation ducts on radar sea return," *Proc. Inst. Elect. Eng. Radar and Signal Processing*, vol. 137, no. F-2, pp. 80–88, 1990.

Caglar Yardim (S'98–M'08) was born in Ankara, Turkey, on December 5, 1977. He received the B.S. and M.S. degrees in electrical engineering from the Middle East Technical University (METU), Ankara, Turkey, in 1998 and 2001, respectively, and the Ph.D. degree in electrical engineering from the University of California, San Diego, in 2007.

From 1998 to 2000, he was a Research Assistant at METU. From 2000 to 2002, he was a Research Engineer in the Microwave and System Technologies Division, ASELSAN Electronic Industries Inc. From 2002 to 2007, he was a Graduate Research Associate at the Marine Physical Laboratory (MPL), Scripps Institution of Oceanography, University of California, San Diego (UCSD). He is currently a Postdoctoral Scholar at MPL/UCSD. His research interests include propagation, optimization, modeling, and inversion of electromagnetic and acoustic signals.

Dr. Yardim was the recipient of the Best Student Paper Award at the 2007 IEEE Radar Conference.

Peter Gerstoft received the M.Sc. and Ph.D. degrees from the Technical University of Denmark, Lyngby, Denmark, in 1983 and 1986, respectively, and the M.Sc. from the University of Western Ontario, London, Canada, in 1984.

From 1987 to 1992 he was with Ødegaard and Danneskiold-Samsøe, Copenhagen, Denmark, working on forward modeling and inversion for seismic exploration, with a year as Visiting Scientist at the Massachusetts Institute of Technology, Cambridge. From 1992 to 1997, he was a Senior Scientist at SACLANT Undersea Research Centre, La Spezia, Italy, where he developed the SAGA inversion code, which is used for ocean acoustic and electromagnetic signals. Since 1997, he has been with the Marine Physical Laboratory, Scripps Institution of Oceanography, University of California, San Diego. His research interests include global optimization, modeling, and inversion of acoustic, elastic and electromagnetic signals.

Dr. Gerstoft is a Fellow of Acoustical Society of America and an elected member of the International Union of Radio Science, Commission F.

William S. Hodgkiss (S'68–M'75) was born in Bellefonte, PA, on August 20, 1950. He received the B.S.E.E. degree from Bucknell University, Lewisburg, PA, in 1972, and the M.S. and Ph.D. degrees in electrical engineering from Duke University, Durham, NC, in 1973 and 1975, respectively.

From 1975 to 1977, he worked with the Naval Ocean Systems Center, San Diego, CA. From 1977 to 1978, he was a faculty member in the Electrical Engineering Department, Bucknell University, Lewisburg. Since 1978, he has been a member of the Faculty, Scripps Institution of Oceanography, University of California, San Diego, and on the staff of the Marine Physical Laboratory, where he is currently Deputy Director. His present research interests are in the areas of adaptive array processing, propagation modeling, and environmental inversions with applications of those to underwater acoustics and electromagnetic wave propagation.

Dr. Hodgkiss is a Fellow of the Acoustical Society of America.